



Study of ionospheric responses over China during September 7–8, 2017 using GPS, Beidou (GEO), and Swarm satellite observations

Jun Tang^{1,2} · Xin Gao¹ · Yinjian Li¹ · Zhengyu Zhong¹

Received: 16 May 2021 / Accepted: 22 February 2022 / Published online: 8 March 2022
© The Author(s), under exclusive licence to Springer-Verlag GmbH Germany, part of Springer Nature 2022

Abstract

The ionospheric responses over China during the geomagnetic storm on September 7–8, 2017 are investigated by using the Global Positioning System (GPS) observations from the Crustal Movement Observation Network of China (CMONOC), the geostationary earth orbit (GEO) satellite observations of BeiDou Navigation Satellite System (BDS) from the IGS Multi-GNSS experiment (MGEX), ionosonde data and Swarm satellite observations. We analyze the vertical TEC (VTEC) variation with a time resolution of 30 s and find that the daytime VTEC shows an enhancement and a positive ionospheric response during the first storm on September 8 over low mid-latitude regions. The critical frequency (f_oF_2) also presents positive deviations during the first storm over mid-latitude areas. In addition, the intense perturbations of the f_oF_2 from station SANY and the GEO VTEC from stations LHAZ and CMUM effectively detect the presence of the traveling ionospheric disturbances (TIDs) during the second storm period. Also, a dense station network observed both equatorward and poleward large-scale TIDs in the southwest of China on the night of September 8. The variation of the electron density N_e from the Swarm A and C satellites verifies the occurrence of these LSTIDs over China. In addition, the auroral oval boundary from DMSP/SSUSI data and the horizontal component of the earth's magnetic field from magnetometers are used to analyze the possible links with these LSTIDs during this geomagnetic storm.

Keywords GPS/BDS observations · Ionospheric response · TEC · Large-scale traveling ionospheric disturbance (LSTID)

Introduction

The coupling of solar wind, magnetosphere, and ionosphere can cause intense disturbance of the ionosphere during geomagnetic storms (Gonzalez et al. 1994). Thus, the ionospheric response during geomagnetic storm has drawn much attention in the space weather field. In addition, the factors, such as local time, sunlit region, storm duration, and secondary excited perturbation, seasonal variation, as well as meteorological conditions, are also associated with the global and regional ionospheric responses (Tang et al. 2015; Yao et al. 2016; Jin et al. 2018; Cherniak and Zakharenkova

2018b; Jonah et al. 2018; Liu et al. 2020a). The ionosphere can respond differently to a storm. One of the responses is the positive or negative ionospheric responses from the variation of TEC or electron density (Matamba et al. 2015; Lei et al. 2018). A wave-like perturbation in ionospheric TEC and electron density is another kind of ionospheric response to the geomagnetic storm. The large-scale traveling ionospheric disturbances (LSTIDs) and medium-scale traveling ionospheric disturbances (MSTIDs) are different kinds of TIDs in terms of propagated period and wavelength (Ding et al. 2011; Huang et al. 2018; Liu et al. 2019). Studying the physical mechanism of ionospheric disturbances and detecting the variations of ionospheric responses to the geomagnetic storm can help us understand the temporal–spatial changes of the ionosphere.

Two consecutive magnetic storms occur during September 7–8, 2017 (Yasyukevich et al. 2018; Zhang et al. 2019a, b). The shock wave of the coronal mass ejection (CME) and the CME's material arrival at the earth are regarded as the main causes to induce these two geomagnetic storms (Blagoveshchensky et al. 2019). Jiang et al. (2020) have

✉ Jun Tang
townjun@gmail.com

¹ School of Civil Engineering and Architecture, East China Jiaotong University, Nanchang 330013, China

² State Key Laboratory of Geodesy and Earth's Dynamics, Innovation Academy for Precision Measurement Science and Technology, Chinese Academy of Sciences, Wuhan 430077, China

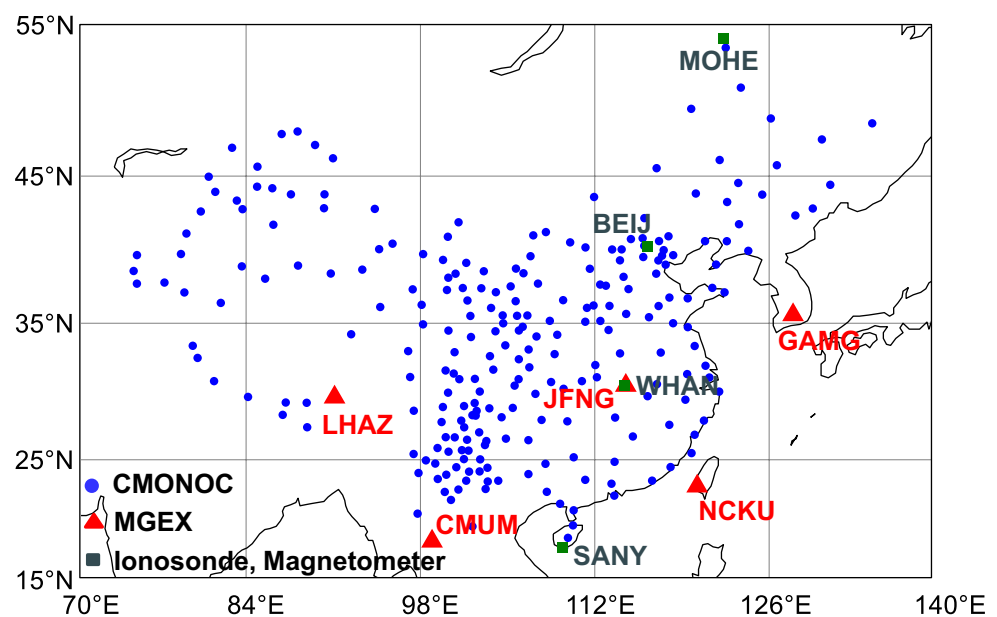
observed the large-scale ionospheric irregularities over the south of China on September 8, 2017, by ionosonde data and demonstrated that an eastward electric field stimulated these low-latitude irregularities. Kumar and Kumar (2020) have investigated ionospheric scintillations over equatorial regions under the space weather in September 2017, and results showed that the positive ionospheric response was associated with joint effects of prompt penetration electric fields (PPEF) and suddenly increasing extreme ultraviolet (EUV) radiations from solar wind. Habarulema et al. (2020) have focused on the ionospheric response over Europe and South Africa regions during a geomagnetic storm on September 7–8, and found that the positive deviations of ionospheric TEC in southern hemisphere mid-latitudes were much larger than the response level in the northern hemisphere on September 8. Alfonsi et al. (2021) have observed the occurrence of equatorial plasma bubbles (EPB) over the India sector and the northward movement of EPB was likely triggered by an enhancement of equatorial electrojet (EEJ) during storm period on September 8. Liu et al. (2020b) have investigated the MSTIDs and large-scale plasma depletions induced by the geomagnetic storm on September 8, 2017 over America; the PPEF and poleward neutral wind were the main reasons to cause the plasma depletions in USA. Akala et al. (2020) observed the longitudinal dependence of ionospheric responses over ocean regions to the storm on September 8. They found a comparative dominance of TEC intensities over the oceans than the landlocked areas. Ferreira et al. (2020) have observed more frequent LSTIDs with higher amplitude during periods of enhanced auroral activity at high latitudes. Lei et al. (2018) have used multiple observations to study the ionospheric disturbances in the Asian–Australian sectors in September 2017 and found that

the presence of long-duration daytime TEC increases during the storm main phase and recovery phase. Li et al. (2018) found that the storm-enhanced equatorial plasma bubbles (EPBs) irregularities extended to dip latitudes of 30°N and 46°N along with rapid sunset F layer height rises during two strong storm periods. Most studies have only focused on a single type of ionospheric response during this storm. The two geomagnetic storms occur at day and night respectively in local time over China, which would cause different types of ionospheric responses in these periods. This present work aims to analyze the diverse ionospheric responses and the results of multiple types of observations performed at low- and mid-latitude areas of China during this geomagnetic storm on September 7–8, 2017.

Data and methods

The GPS observation data from nearly 250 stations of the Crustal Movement Observation Network of China (CMONOC), the geostationary earth orbit (GEO) satellite data of BeiDou Navigation Satellite System (BDS), the ionosonde and magnetometer data collected from 4 stations in China are used to investigate the ionospheric responses over China. Figure 1 shows the locations of CMONOC stations (blue circles), the IGS Multi-GNSS experiment (MGEX) stations (red triangles), ionosonde and magnetometer stations (green squares) over China and surrounding areas. Based on the observation data from CMONOC stations, we calculate the ionospheric delay by the geometry-free combination used in double-frequency GNSS receivers for precise point positioning (PPP) method and convert the slant TEC (STEC) to the vertical TEC (VTEC) on all ionospheric

Fig. 1 Locations of CMONOC, MGEX stations, ionosonde and magnetometer stations



pierce points (IPPs) based on the ionospheric single-layer model. Considering the influence of TEC background trend, we filter it to obtain actual TEC perturbation named detrended TEC (DTEC) by regarding the background trend as a second-order function of universal time and latitude referring to the previous studies (Ding et al. 2012; Tang et al. 2016). The DTEC can be given as:

$$\begin{aligned} \text{DTEC} &= \text{VTEC} - \overline{\text{VTEC}} \\ &= \text{VTEC} - (C_0 + C_1(\varphi - \varphi_0) + C_2(\varphi - \varphi_0)^2 \\ &\quad + C_3(t - t_0) + C_4(t - t_0)^2), \end{aligned} \quad (1)$$

where VTEC, $\overline{\text{VTEC}}$ represent the measured VTEC from GPS observations and the TEC background trend, respectively; φ , t are the geographic latitude and universal time, respectively; represents the universal time at the minimum of the zenith distance at the ionospheric pierce point (IPP); is the latitude of the IPP at time; $C_0 \sim C_4$ are the coefficients of the function.

The BDS GEO VTEC data from the MGEX stations and the critical frequency (foF_2) of the ionospheric F_2 layer from ionosonde stations are used to analyze the variation and disturbance of the ionosphere. The day-to-day variability threshold of the ionospheric VTEC can be defined as (Jin et al. 2017):

$$r\text{TEC} = \text{TEC}_{\text{median}} \pm 1.5\text{std}, \quad (2)$$

where $r\text{TEC}$ represents the regular variability threshold of the TEC; $\text{TEC}_{\text{median}}$ is the median values of 5 days GEO VTEC before the storm time; std is the standard deviation of 5 days VTEC values. Therefore, the outside parts of the regular variability threshold can be seen as the ionospheric response. The relative deviation of foF_2 is used to measure the disturbance intensity of the ionospheric F_2 layer. It can be given as follows:

$$DfoF_2 = \frac{foF_2 - foF_2(\text{median})}{foF_2(\text{median})}, \quad (3)$$

where foF_2 is the measurement from ionosonde station during storm time; $foF_2(\text{median})$ represent the median values in 5 days measurements before storm time (Wen and Mei 2020).

The horizontal intensity of the magnetic field variation observed from the magnetometers with latitude intervals are used to characterize the disturbance response of the earth's magnetic field to the storm. In addition, the electron density Ne of the ionosphere from the Swarm A and C satellites is introduced to analyze the latitude variation of the electron density Ne over China and verify the results of the ionospheric response during storm time. The Swarm is a constellation mission for earth observation launched by European Space Agency (ESA). The mission consists of two lower

pair of satellites A, C flying side by side at 470 km altitude and one higher satellite B flying at 520 km altitude (Akala et al. 2020).

Geomagnetic conditions of the storm in September 2017

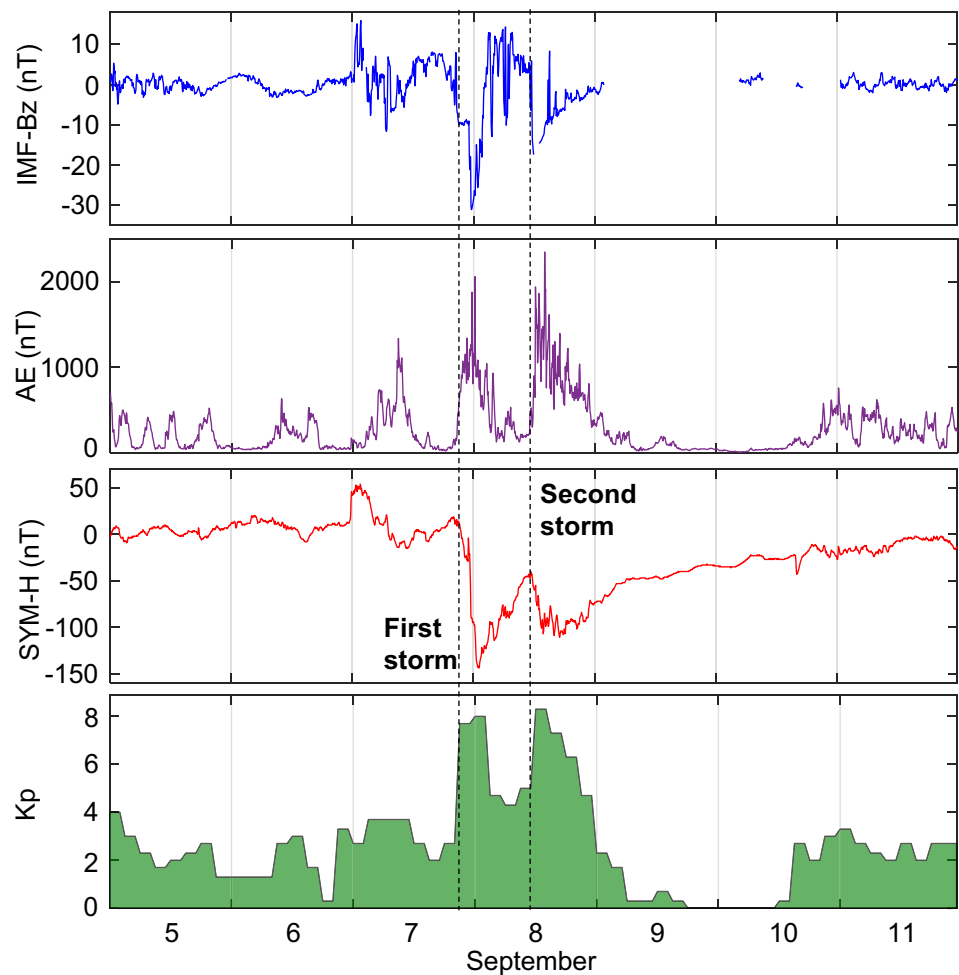
Many studies have discussed the geomagnetic activity condition on September 7–8, 2017 (Curto et al. 2018; Habarulema et al. 2020; Kumar and Kumar 2020). We briefly describe the evolution of the storm and the main factors that cause geomagnetic disturbance. Figure 2 shows the variations of the Bz component of the interplanetary magnetic field (IMF Bz), the auroral electrojet index (AE), the geomagnetic indexes SYM-H and Kp during September 5–11, 2017. The first storm starts at 20:00UT on September 7 with a rapidly southward turning of IMF Bz and a sudden decline of SYM-H index. The IMF Bz and SYM-H index reach the minimum values of -31.0 nT and -144 nT at 01:00 UT on September 8, which is generally attributed to the coronal mass ejection (CME) (Blagoveshchensky et al. 2019). The AE and Kp indexes also reached the peak value of 2063 nT and 8. The IMF Bz and SYM-H index turn to the minimum values again of -17.4 nT and -107 nT respectively at 13:50 UT on September 8, which characterizes the second geomagnetic storm as a result of the CME's material arrival (Blagoveshchensky and Sergeeva 2019). The AE and Kp index also display the second peak values of 2351 nT and 8 at that moment. Then the second storm has gradually recovered the regular condition on September 9–11.

Fluctuation of ionospheric TEC

Figure 3 shows the variation of VTEC with a temporal interval of 2 h observing from nearly 250 CMONOC stations on September 8, 2017. The ionospheric VTEC displays a prominent enhancement and reaches the maximum value of 47 TECU at 03:00 UT at mid-latitudes, while VTEC values reach the maximum value of 66 TECU at 05:00 UT at the low-latitude regions. After 13:00 UT on September 8, the VTEC shows a significant depletion and decreases to the minimum at low and mid-latitude regions. Considering the variation of geomagnetic conditions on September 8, the ionospheric VTEC enhanced during the first storm over China regions. After that, the VTEC generates a rapid depletion during the second storm.

Figure 4 shows the latitude variations of VTEC along geographical longitudes (100°E , 110°E) during September 6–10, 2017. The lower panel presents the variation of SYM-H index and black dashed lines represent the time of the first storm and the second storm. Figure 5 shows the longitude variations of VTEC along geographical latitudes (25°N , 30°N) during September 6–10, 2017. The lower

Fig. 2 Variations of Bz component of interplanetary magnetic field (IMF), auroral electrojet (AE), geomagnetic indexes SYM-H and Kp on September 5–11, 2017. The vertical dotted lines represent the time of the first storm and the second storm



panel and black dashed lines in Fig. 5 are the same as Fig. 4. From Fig. 4, VTEC values decrease with the increase of latitude, and its variation over geographical longitudes (100°E , 110°E) has a similar identity during September 6–10. During the first storm on September 8, the mid-latitude VTEC displays a prominent increase compared to the value on September 6–7. By contrast, the low-latitude VTEC has an unusual variation that shows a persistent enhancement of VTEC values at daytime on September 8–10 during this geomagnetic storm. In Fig. 5, the longitude variations of VTEC show considerable disparities over different latitudes (25°N , 30°N). The VTEC values over latitude 30°N increase to the maximum during the first storm and then display a rapid depletion during the second storm. We observe a different change of VTEC over latitude 25°N . The VTEC values reach the peak value on September 7 before the storm time, whereas its values present a moderate decrease during the first storm on September 8. During September 9–10, the VTEC over 25°N shows a persistent enhancement compared to the values over latitude 30°N .

Figure 6 shows the variations of VTEC observed from BDS GEO satellites over 5 MGEX stations during

September 6–10, 2017. The dark and light blue dashed lines represent the regular variability threshold calculated from (2). The part that is larger (smaller) than the regular threshold is defined as the positive (negative) response, respectively. As shown in Fig. 6, the daytime VTEC values from stations GAMG and JFNG present a marked increase to 47 TECU at 05:00 UT (13:00 LT) on September 8 and display distinct positive responses with disturbances up to 15–20 TECU during the first storm. The VTEC values over these two stations all show slightly negative responses at nighttime on September 9–10, consistent with Lei et al. (2018). At station LHAZ, TEC displays a unique variation feature that the maximum of VTEC values occurs on September 7 before the storm time, which is similar to the result in Fig. 5. During the first storm, the daytime VTEC from station LHAZ showed no obvious disturbance compared to September 7. From the result of stations NCKU and CMUM, the daytime VTEC values present moderate positive responses during the first storm, but the VTEC values from station CMUM show a distinct positive response on September 9 after the second storm. In addition, we discover the nighttime VTEC values generate some intensive perturbations observed from

Fig. 3 TEC maps calculated from CMONOC stations from 01:00 UT to 23:00 UT on September 8, 2017

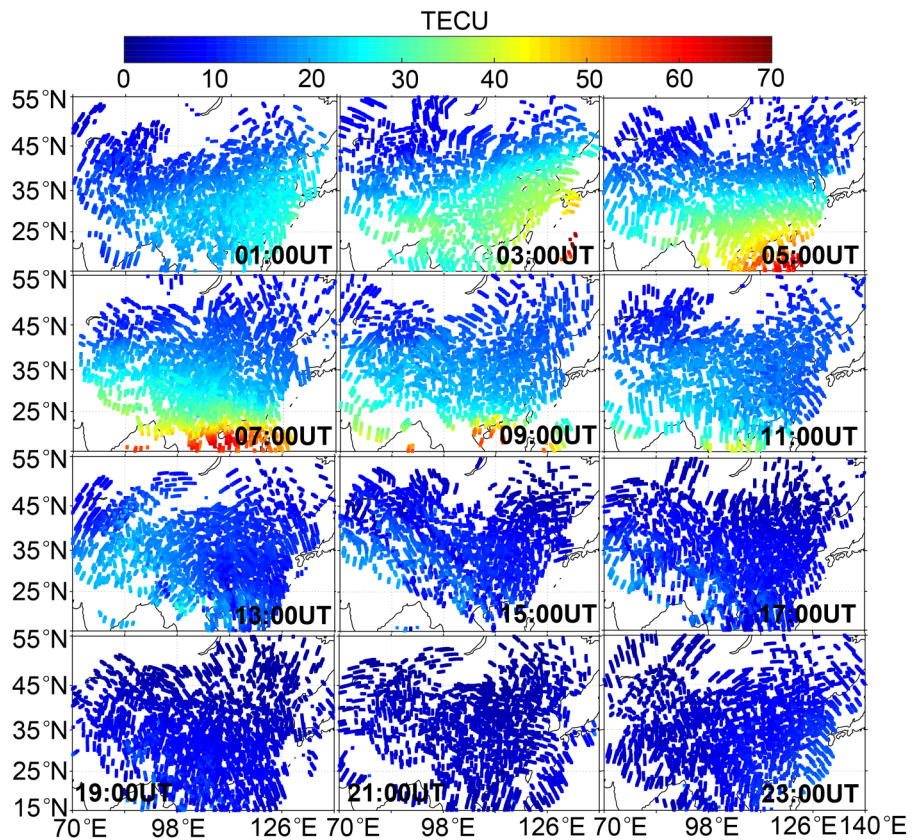
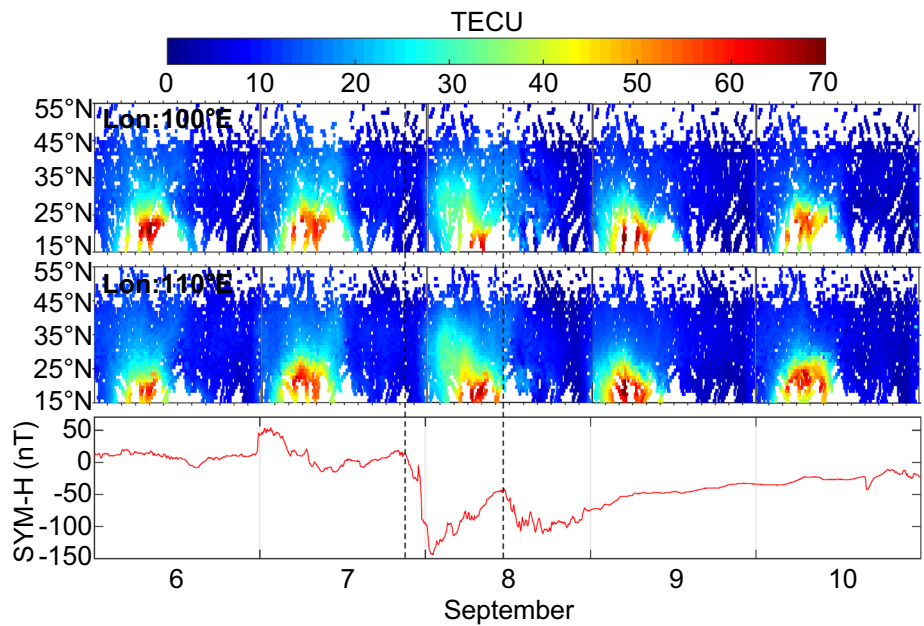


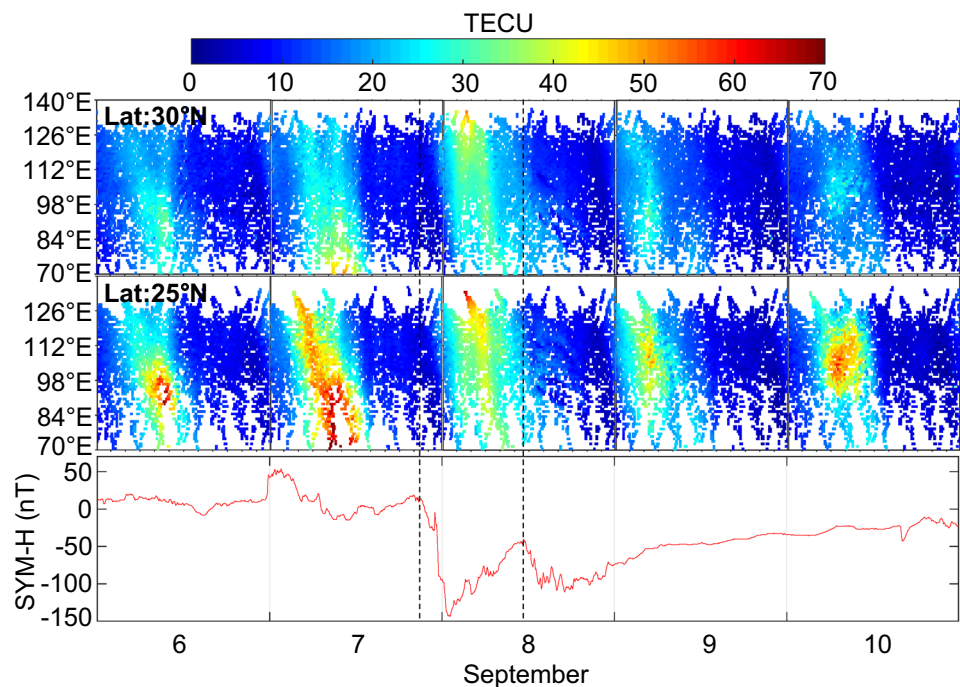
Fig. 4 Latitude variations of VTEC along geographical longitudes (100°E, 110°E) during September 6–10, 2017. The lower panel presents the variation of SYM-H index



stations LHAZ and CMUM during the second storm time on September 8, which means that the ionosphere in this area might generate a different response during the nighttime compared to the regular variation of VTEC from other stations.

Figure 7 shows the variations of foF_2 and their median values in the 5 days measurements before the storm time at stations BEIJ, WHAN, and SANY. Figure 8 displays the variations of $DfoF_2$ at three stations marked by different colors. During the first storm, the variations of foF_2 observed from

Fig. 5 Longitude variations of VTEC along geographical latitudes (25°N, 30°N) during September 6–10, 2017



stations BEIJ and WHAN show distinct enhancement up to nearly 8 MHz and 11 MHz, respectively in Fig. 7, and the $DfoF_2$ of them present positive deviations compared to the normal state marked by green and blue lines in Fig. 8. The results from stations BEIJ and WHAN are similar to the variations of VTEC values from stations GAMG and JFNG, demonstrating that positive ionospheric response occurs at mid-latitude areas during the first storm time September 7–8, 2017. The foF_2 from station SANY has a similar variation with the median value and the $DfoF_2$ from it has no clear disturbance deviations during the first storm time. But the $DfoF_2$ display a moderate positive deviation during the second storm on September 9 as shown in Fig. 8. We suggest that the low-latitude ionosphere has no distinct response during the first storm time compared to the mid-latitude areas, while it has a positive response after the second storm on September 9, 2017 from the results of stations CMUM and SANY.

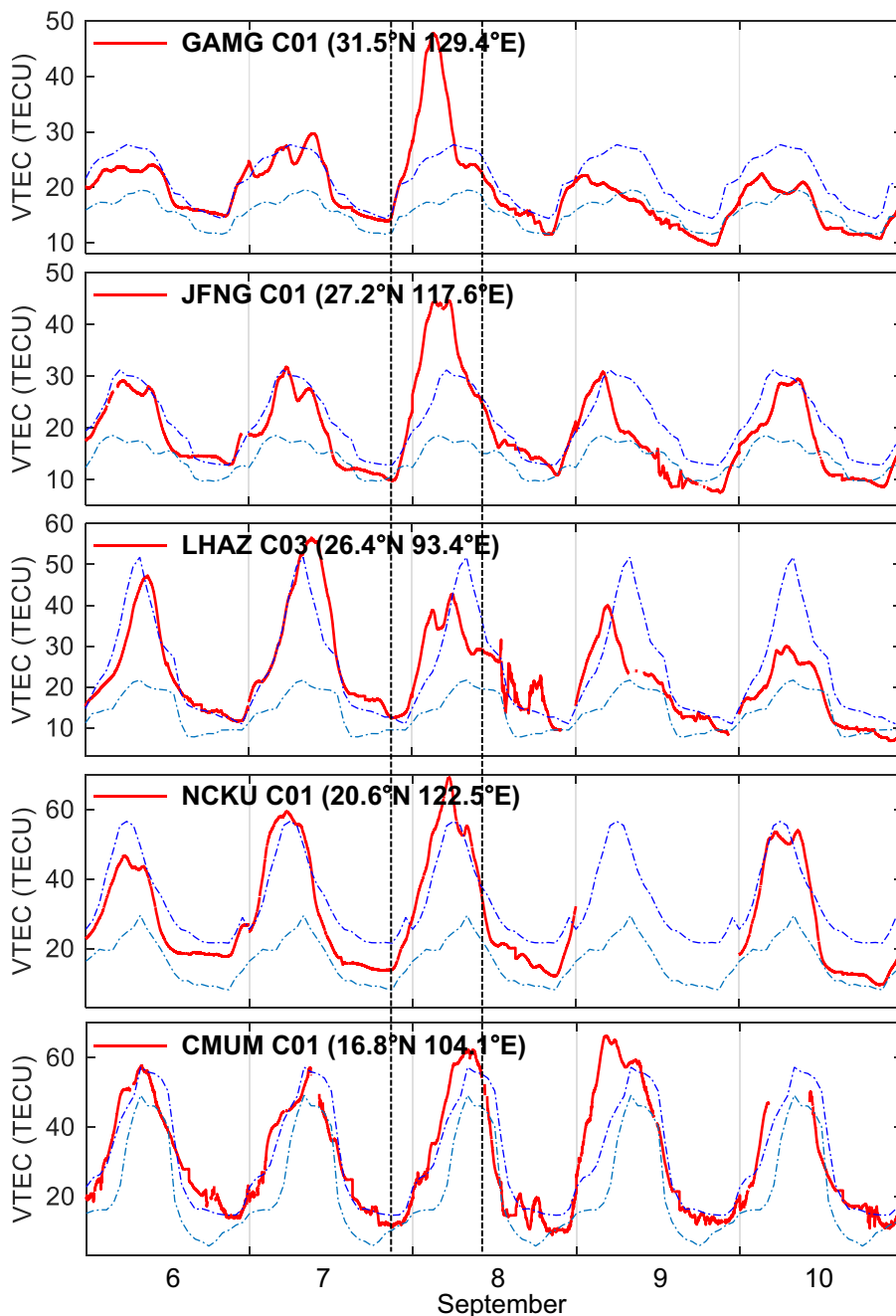
During the second storm time on September 8, the foF_2 from stations SANY also presents intensive perturbations that are the same as the variations of VTEC from stations LHAZ and CMUM. According to the locations of these stations, we speculate that this anomaly perturbation mainly occurs in the southwest of China. Therefore, the DTEC from dense CMONOC stations are used to study this anomaly in the following text.

Large-scale traveling ionospheric disturbances

From the characteristic disturbance of the VTEC and foF_2 during the second storm period, we further plot two-dimensional de-trended TEC maps to investigate the occurrence of the LSTIDs over China by eliminating TEC background trends. Figure 9 shows the variations of Detrended TEC (DTEC) maps over China from 14:00 UT to 17:00 UT on September 8. The four black dotted lines setting along the meridional and zonal lines as 100°E(a), 105°E(b), 35°N(c) and 25°N(d) are used to specifically investigate the meridional and zonal variations of DTEC on these four axes with universal time during the storm period. As shown in Fig. 9, we find a drastic LSTID event lasting for more than 3 h on September 8. The propagation scope mainly covers the most southwest regions of China, ranging from 90°E to 115°E, 20°N to 40°N. Considering the irregular changes of the LSTID, we think that this irregular characteristic possibly is attributed to the joint effect of multiple LSTID groups.

Figure 10 presents the DTEC variations in the time-latitude along 100°E, 105°E longitude axes. The time axes are presented by universal time (UT) and local time (LT = UT + 8 h). Figure 11 shows the DTEC variations in the time longitude along 35°N and 25°N latitude axes. The black dashed lines mark the LSTID front trajectory in Figs. 10 and 11. We have observed two kinds of LSTID groups on September 8. In particular, the first group of LSTID occurs at about 13:30 UT (21:30 LT) and

Fig. 6 Variations of VTEC from GEO satellites on September 6–10, 2017. The red lines represent the GEO VTEC from 5 MGEX stations in the order of the IPPs from north to south. The dark and light blue dashed lines represent the regular variability threshold



lasts for more than 3 h until 17:00 UT (01:00 LT). This kind of LSTID propagates equatorward from 42 to 28°N accompanied by a positive and a negative propagation front. The zonal velocity of this LSTID reaches about 132.3 m/s. Another LSTID marked group 2 in Fig. 10 starts at nearly 16:30 UT (00:30 LT) and lasts until 19:00 UT (03:00 LT), which propagates with a period of 2.5 h. The propagated direction of the second LSTID is poleward from 15 to 26°N with one negative and two positive propagation fronts. The zonal velocity of this LSTID is about 149.7 m/s. We have also observed the longitude propagation features of corresponding two LSTID groups along 35°N

and 25°N latitude axes in Fig. 11. The propagated directions of these two LSTIDs along 35°N and 25°N latitude axes are both westward. The first one propagates from 107 to 96°E with a meridional velocity of 103.9 m/s, and the other propagates from 115 to 98°E with a meridional velocity of 224.9 m/s.

Considering the propagation velocity of LSTID fronts in Figs. 10, 11 is not the real velocity movement of LSTID. According to the geometric structure, the zonal and meridional velocities are viewed as the vertical and horizontal components of actual movement vectors of LSTID propagation (Chen et al. 2020). The propagation azimuth θ of actual

Fig. 7 Variations of f_oF_2 from three ionosonde stations BEIJ (40.3°N, 116.2°E), WHAN (30.5°N, 114.4°E), SANY (18.3°N, 109.4°E) on September 6–10, 2017. The blue lines represent the median values in 5-days f_oF_2 measurements before the storm time

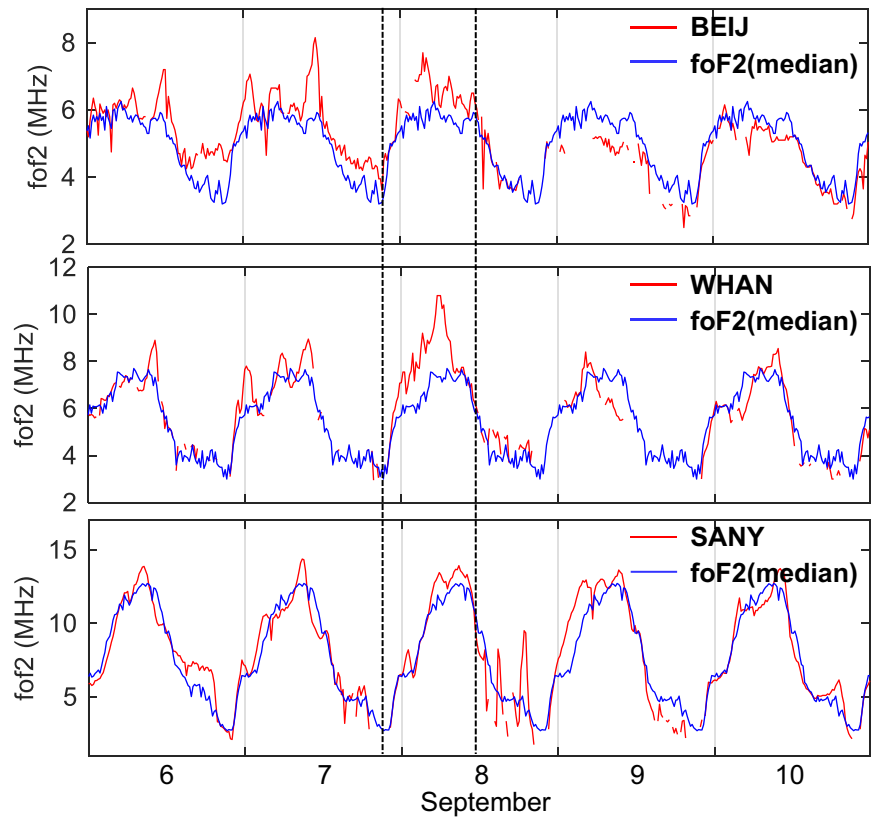
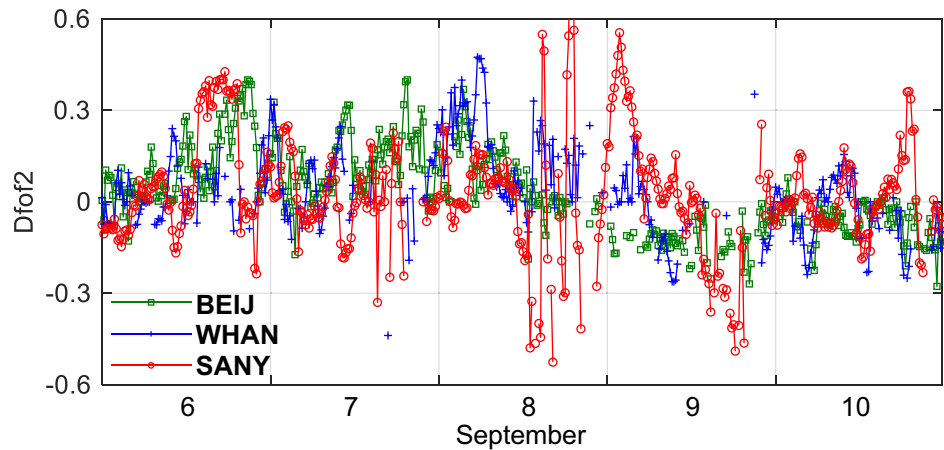


Fig. 8 Variations of $DfoF_2$ calculated from three ionosonde stations on September 6–10, 2017



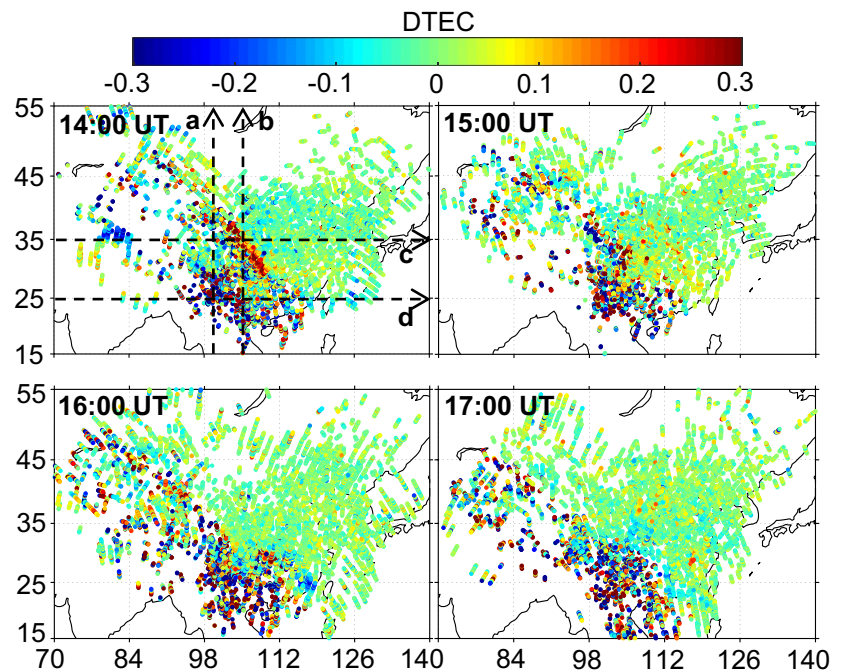
LSTID velocity can be regarded as the arctan function of vertical and horizontal components. Therefore, the actual LSTID velocity and the propagation azimuth can be given as follows:

$$\begin{cases} V_{TID} = V_{vertical} \times V_{horizontal} / \sqrt{V_{vertical}^2 + V_{horizontal}^2} \\ \theta = \arctan(V_{vertical} / V_{horizontal}) \end{cases} \quad (4)$$

where V_{TID} , θ represent the actual velocity and propagation azimuth of LSTID, respectively. Based on the above method, the actual velocity and propagation azimuth of the first LSTID group that occurs at 13:30 UT is 81.7 m/s and 231.8°, respectively. The propagation parameters of the second LSTID group over the low-latitude areas are 124.6 m/s and 326.3°, respectively.

Figure 12 presents the variations of the electron density N_e observed from the Swarm A and C satellites in the evening sector on September 6 and 8, 2017. The N_e of September

Fig. 9 Variations of de-trended TEC (DTEC) maps from 14:00 UT to 17:00 UT on September 8, 2017. The four axes are the meridional and zonal lines of 100°E (a), 105°E (b), 35°N (c) and 25°N (d)



6 is regarded as the regular level reference to analyze the disturbed variation of Ne from Swarm A and C during storm time. It can notice that the low-latitude Ne from Swarm A and C both present prominent perturbations at 15:28 UT on September 8 compared to the values at 15:12 UT on September 6. At 16:59 UT on September 8, the intensity of the Ne perturbations along longitude about 75°E decays clearly with time compared to the values along longitude about 100°E. Based on the above results, the perturbations of the low-latitude Ne mainly occur in the southwest of China during the second storm time, which is almost consistent with the scope and time of the LSTID in Fig. 9. The in situ electron density Ne measured by the Swarm A and C satellites verifies the presence of the nighttime LSTID in the southwest of China during the second storm period on September 8.

Based on de-trended TEC maps calculated from CMONOC stations, we can observe the propagated features of the LSTIDs in detail over China. In Figs. 9, 10, 11, the first group of LSTID propagates with equatorward direction and the second group of LSTID with poleward direction. The sources of equatorward LSTIDs have been widely discussed in previous studies (Tang et al. 2016; Zakharenkova et al. 2016; Cherniak and Zakharenkova 2018a, b; Jonah et al. 2018; Zhang et al. 2019a, b; Chen et al. 2020). It has been accepted that the enhancement of auroral electrojet, movement of the auroral oval, particle precipitation in the auroral areas are mainly physical sources of the equatorward LSTID propagation during the geomagnetic storm (Ding et al. 2007; Lyons et al. 2019). In the auroral region during storm time, the joule heating and Loren drag force stimulate

the presence of atmospheric gravity waves (AGW), which contributes to the large-scale TIDs from high latitudes to lower latitudes (Chimonas and Hines 1970; Cherniak and Zakharenkova 2018a). Figure 13 shows the positions of the equatorward auroral oval boundary in the northern hemisphere on September 8 from DMSP/SSUSI data. Different colors represent the positions of the auroral oval at different time period. It can notice that the auroral oval boundary gradually moves equatorward from 12:20 to 14:46 UT on September 8, which is clearly observed in the north of China. The equatorward LSTID at 13:30 UT is also observed along with an equatorward propagation. The features of this LSTID are well consistent with the variation of the auroral oval boundary from 12:20 to 14:46 UT in Fig. 13. The above results demonstrate that the movement of the auroral oval possibly induces the equatorward LSTID during the second storm on September 8.

Compared to the equatorward LSTID, studies on poleward LSTID are relatively less than equatorward and the physical mechanism of poleward LSTID is also complicated. Chen et al. (2020) have investigated some poleward LSTIDs occurring in June 2015 over China and discovered that only one of the poleward LSTIDs is excited in the auroral oval directly according to the movement of the auroral oval during storm time. The sources of other poleward LSTIDs are not sure due to a lack of observational data. Jonah et al. (2018) have observed both equatorward and poleward medium-scale TIDs over North America in May 2017 and they believed that the poleward-propagating TID possibly was attributed to local atmospheric gravity wave generating from convection activities. Habarulema et al. (2015) have

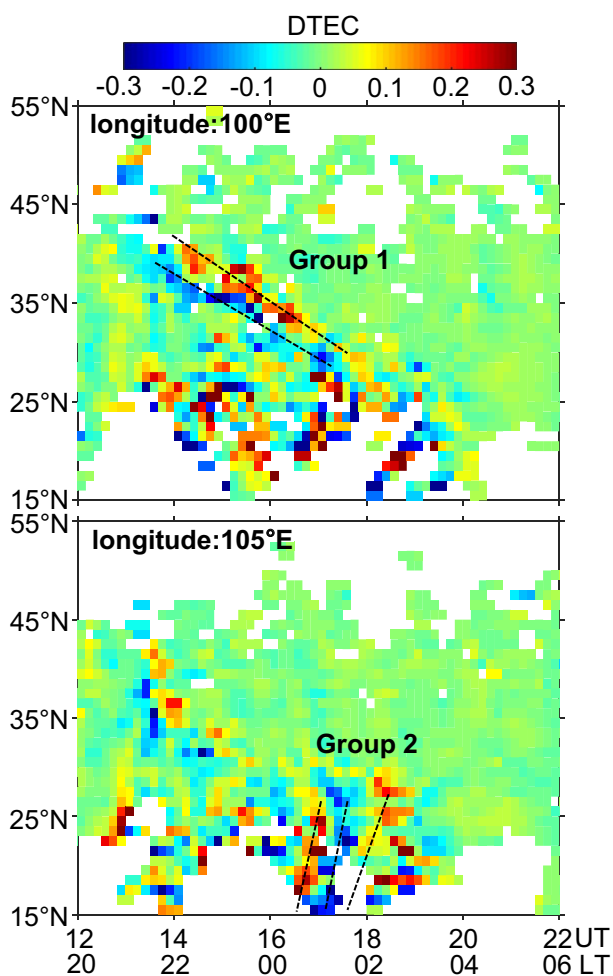


Fig. 10 Variations of de-trended TEC (DTEC) maps in the time-latitude along 100°E, 105°E longitude axes. The black dashed lines represent the propagation of different LSTIDs

first observed poleward traveling ionospheric disturbances during the geomagnetic storm over African sectors and they thought the poleward-propagating LSTIDs were associated with the equatorial electrojet and the expansion of equatorial ionization anomaly (EIA).

The geomagnetic indices in Fig. 2 are the averaged values by data from stations located at different regions. But the local magnetometers can effectively observe their own characteristic features of the magnetic field variations. Figure 14 presents the variations of the H component of the earth’s magnetic field variations over three magnetometers during September 7–9. The data sets are available for stations MOHE, BEIJ and SANY. It can be seen that the H components of the three stations all decrease to the minimum at 01:00 UT on September 8 during the first storm period, which is almost synchronous with the variations of the geomagnetic indices in Fig. 2. During the second storm period, the disturbance intensity of the H component at

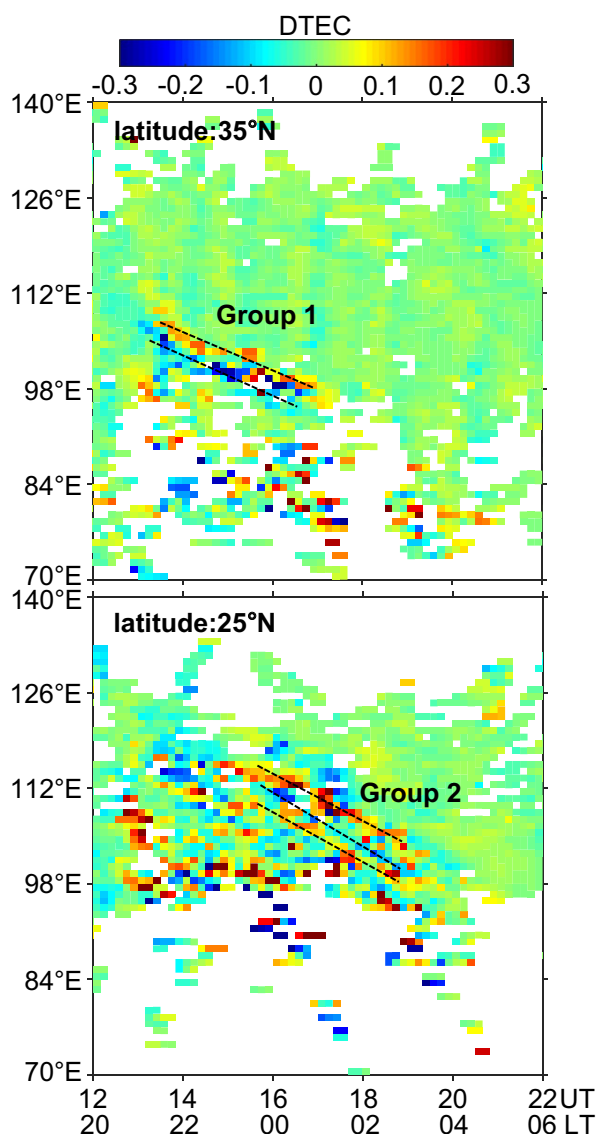
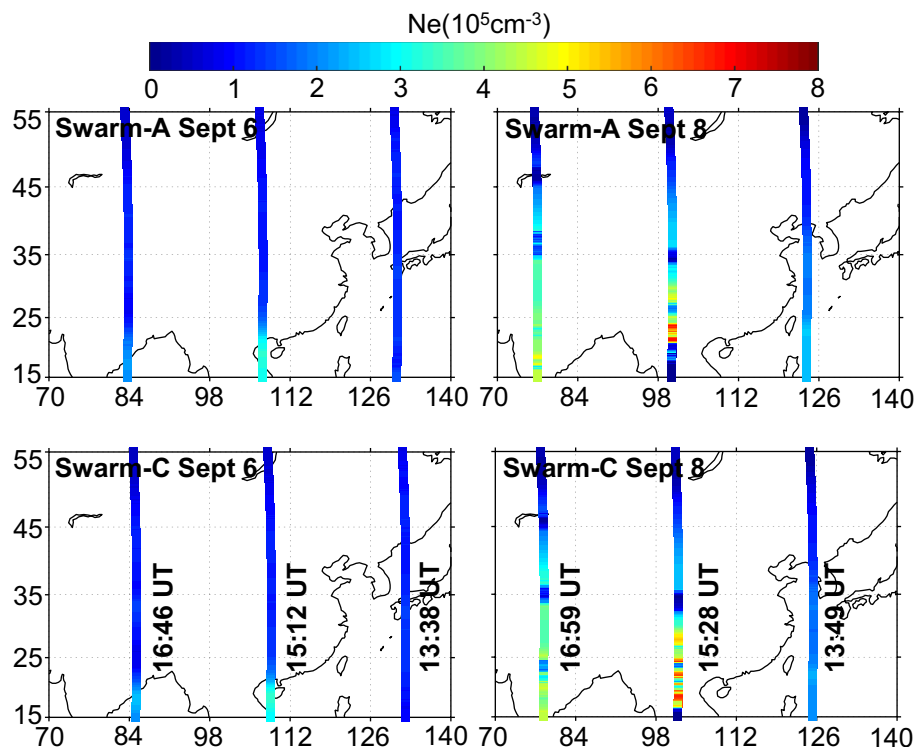


Fig. 11 Variations of de-trended TEC (DTEC) maps in the time-longitude along 35°N, 25°N latitude axes

SANY magnetometer is equivalent to the intensity during the first storm. The disturbance intensity of three magnetometers gradually weakens from low to high latitude compared to the first storm period. Based on the results from the H component, we demonstrate that the magnetic field at the low-latitude area had a more intense disturbance during the second storm on September 8, which possibly interconnects with the occurrence of the poleward LSTID.

Fig. 12 Electron density N_e from the Swarm A (top) and Swarm C (bottom) satellites on September 6, 8 at different time



Conclusion

We investigate the different ionospheric responses over China during the two consecutive geomagnetic storms on September 7–8, 2017 by combining GPS, GEO, Swarm satellites, ionosonde and magnetometer observations. The results show that the low- and mid-latitude VTEC present an enhancement and positive disturbance responses during the first storm period. The intensity of the positive response weakens with the latitude decrease. The foF_2 only presents positive deviations over mid-latitude areas during the first storm. During the second storm, the pronounced perturbations observed from the VTEC and foF_2 in the southwest of China are regarded as the signature of the TID event. The occurrences of both equatorward and poleward LSTIDs are observed during the second storm period on the night of September 8. The corresponding duration of equatorward and poleward LSTIDs is about 3.5 h and 2.5 h, respectively, and these LSTIDs observed from GPS are consistent with the period of the perturbations from GEO VTEC and foF_2 . The electron density N_e along longitude 100°E observed from Swarm A and C satellites also presents comparative perturbations like the VTEC and foF_2 during the second storm period, which verifies the presence of the LSTIDs over China. Additionally, the variation of the auroral oval boundary from DMSP/SSUSI data presents an equatorward expansion that is similar to the feature of the equatorward LSTID observed. The horizontal component of the earth's

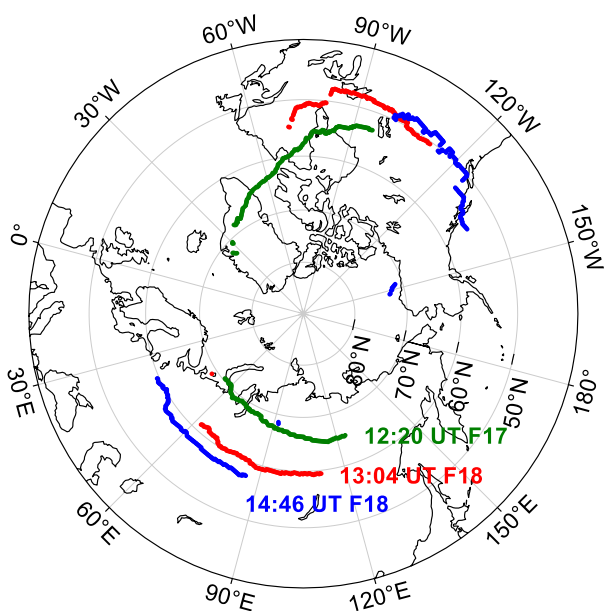
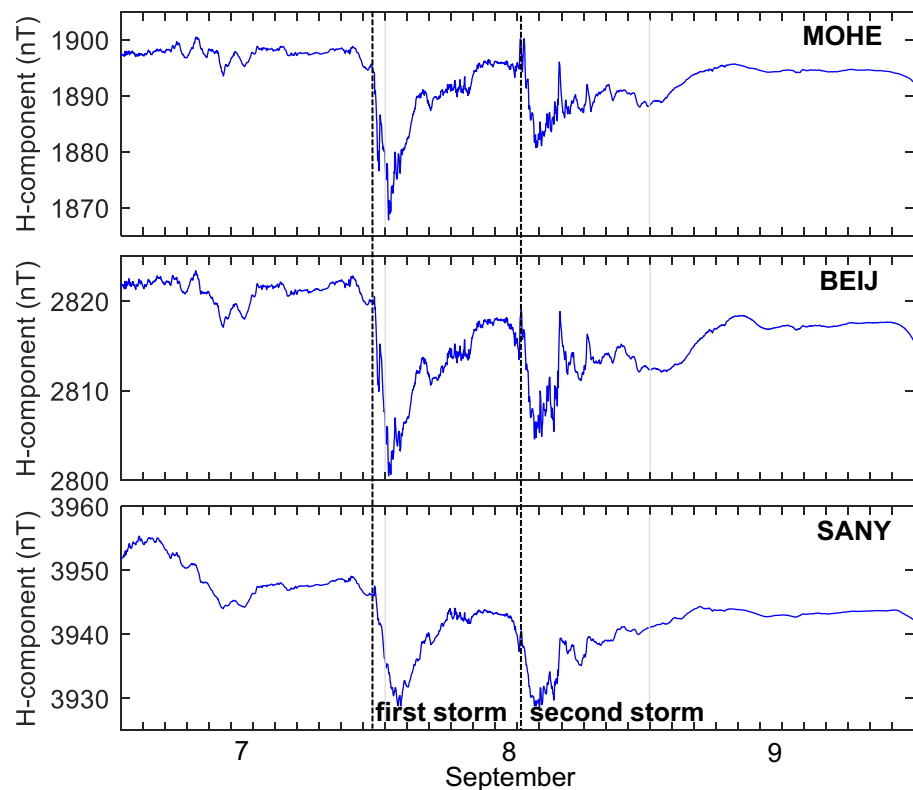


Fig. 13 Position of the auroral oval equatorward boundary in the northern hemisphere at 12:20 UT, 13:04 UT, 14:46 UT on September 8. F17 and F18 represent the satellite numbers from the DMSP data

Fig. 14 Variations of the H component of the earth's magnetic field over MOHE (53.5°N, 122.3°E), BEIJ (40.3°N, 116.2°E), SANY (18.3°N, 109.4°E) magnetometers during September 7–9, 2017



magnetic field at SANY magnetometer has an equivalent disturbance intensity compared to the first storm during the second storm, which possibly interconnects with the presence of the poleward LSTID during the second storm period. From the results of these multiple observations, we demonstrate that the ionospheric responses over China during this peculiar geomagnetic storm performs differently in local time. It mainly performs a positive disturbance response in the daytime during the first storm and two LSTIDs with different propagation directions in the nighttime during the second storm.

Acknowledgements This work is supported by the National Natural Science Foundation of China (41761089). We acknowledge IGS for providing MGEX data, GIRODibase for providing ionosonde data, Beijing National Observatory of Space Environment for providing magnetometer data, OMNIWeb for providing OMNI data, European Space Agency for providing Swarm satellite data, and Johns Hopkins University for providing DMSP/SSUSI data.

Data availability The MGEX data were obtained from the IGS (<ftp://cddis.gsfc.nasa.gov/pub/gps/data/campaign/mgex>), the GPS data from CMONOC, the OMNI data from the GSFC/SPDF OMNIWeb interface (<http://omniweb.gsfc.nasa.gov>), the ionosondes data from GIRODibase (<https://ulcar.uml.edu/>), the magnetometer data from Beijing National Observatory of Space Environment (<http://wdc.geophys.ac.cn>), the Swarm satellite data from the European Space Agency (<http://earth.esa.int/Swarm>), and the auroral oval boundary from DMSP/SSUSI data (<https://ssusi.jhuapl.edu/>).

References

- Akala AO, Oyeyemi EO, Amaechi PO, Radicella SM, Nava B, Amory-Mazaudier C (2020) Longitudinal responses of the equatorial/low-latitude ionosphere over the oceanic regions to geomagnetic storms of May and September 2017. *J Geophys Res Space Phys* 125(8):e2020JA027963. <https://doi.org/10.1029/2020JA027963>
- Alfonsi L, Cesaroni C, Spogli L, Regi M, Paul A, Ray S, Sinha AK (2021) Ionospheric disturbances over the Indian sector during September 8 2017 geomagnetic storm: plasma structuring and propagation. *Space Weather* 19(3):e2020SW002607. <https://doi.org/10.1029/2020SW002607>
- Blagoveshchensky DV, Sergeeva MA (2019) Impact of geomagnetic storm of September 7–8, 2017 on ionosphere and HF propagation: a multi-instrument study. *Adv Space Res* 63(1):239–256. <https://doi.org/10.1016/j.asr.2018.07.016>
- Blagoveshchensky DV, Sergeeva MA, Corona-Romero P (2019) Features of the magnetic disturbance on September 7–8, 2017 by geophysical data. *Adv Space Res* 64(1):71–182. <https://doi.org/10.1016/j.asr.2019.03.037>
- Chen G, Ding F, Wan W, Hu L, Zhao X, Li J (2020) Structures of multiple large-scale traveling ionospheric disturbances observed by dense Global Navigation Satellite System networks in China. *J Geophys Res Space Phys* 125(2):e2019JA027032. <https://doi.org/10.1029/2019JA027032>
- Cherniak I, Zakharenkova I (2018a) Large-scale traveling ionospheric disturbances origin and propagation: case study of the December 2015 geomagnetic storm. *Space Weather* 16(9):1377–1395. <https://doi.org/10.1029/2018SW001869>
- Cherniak I, Zakharenkova I (2018b) Ionospheric total electron content response to the great American solar eclipse of August 21 2017. *Geophys Res Lett* 45(3):1199–1208. <https://doi.org/10.1002/2017gl075989>

- Chimonas G, Hines CO (1970) Atmospheric gravity waves launched by auroral currents. *Planet Space Sci* 18(4):565–582. [https://doi.org/10.1016/0032-0633\(70\)90132-7](https://doi.org/10.1016/0032-0633(70)90132-7)
- Curto JJ, Marsal S, Blanch E, Altadill D (2018) Analysis of the solar flare effects of September 6 2017 in the ionosphere and in the Earth's magnetic field using spherical elementary current systems. *Space Weather* 16(11):1709–1720. <https://doi.org/10.1029/2018SW001927>
- Ding F, Wan W, Ning B, Wang M (2007) Large-scale traveling ionospheric disturbances observed by GPS total electron content during the magnetic storm of 29–30 October 2003. *J Geophys Res Space Phys*. <https://doi.org/10.1029/2006JA012013>
- Ding F, Wan W, Xu G, Yu T, Yang G, Wang JS (2011) Climatology of medium-scale traveling ionospheric disturbances observed by a GPS network in central China. *J Geophys Res Space Phys*. <https://doi.org/10.1029/2011JA016545>
- Ding F, Wan W, Ning B, Zhao B, Li Q, Zhang R, Song Q (2012) Two-dimensional imaging of large-scale traveling ionospheric disturbances over China based on GPS data. *J Geophys Res Space Phys*. <https://doi.org/10.1029/2012JA017546>
- Ferreira AA, Borries C, Xiong C, Borges RA, Mielich J, Kouba D (2020) Identification of potential precursors for the occurrence of Large-Scale Traveling Ionospheric Disturbances in a case study during September 2017. *J Space Weather Space Clim* 10:32. <https://doi.org/10.1051/swsc/2020029>
- Gonzalez WD, Joselyn JA, Kamide Y, Kroehl HW, Rostoker G, Tsurutani BT, Vasyliunas VM (1994) What is a geomagnetic storm? *J Geophys Res Space Phys* 99(A4):5771–5792. <https://doi.org/10.1029/93JA02867>
- Habarulema JB, Katamzi ZT, Yizengaw E (2015) First observations of poleward large-scale traveling ionospheric disturbances over the African sector during geomagnetic storm conditions. *J Geophys Res Space Phys* 120(8):6914–6929. <https://doi.org/10.1002/2015JA021066>
- Habarulema JB, Katamzi-Joseph ZT, Burešová D, Nndanganeni R, Matamba T, Tshisaphungo M, Mahrous A (2020) Ionospheric response at conjugate locations during the 7–8 September 2017 geomagnetic storm over the Europe–African longitude sector. *J Geophys Res Space Phys* 125(10):e2020JA028307. <https://doi.org/10.1029/2020JA028307>
- Huang F, Lei J, Dou X, Luan X, Zhong J (2018) Nighttime medium-scale traveling ionospheric disturbances from airglow imager and Global Navigation Satellite Systems observations. *Geophys Res Lett* 45(1):31–38. <https://doi.org/10.1002/2017GL076408>
- Jiang C, Wei L, Yang G, Aa E, Lan T, Liu T, Zhao Z (2020) Large-scale ionospheric irregularities detected by ionosonde and GNSS receiver network. *IEEE Geosci Remote S*. <https://doi.org/10.1109/LGRS.2020.2990940>
- Jin S, Jin R, Kutoglu H (2017) Positive and negative ionospheric responses to the March 2015 geomagnetic storm from BDS observations. *J Geod* 91(6):613–626. <https://doi.org/10.1007/s00190-016-0988-4>
- Jin H, Zou S, Chen G, Yan C, Zhang S, Yang G (2018) Formation and evolution of low-latitude F region field-aligned irregularities during the 7–8 September 2017 storm: Hainan coherent scatter phased array radar and digisonde observations. *Space Weather* 16(6):648–659. <https://doi.org/10.1029/2018SW001865>
- Jonah OF, Coster A, Zhang S, Goncharenko L, Erickson PJ, de Paula ER, Kherani EA (2018) TID observations and source analysis during the 2017 Memorial Day weekend geomagnetic storm over North America. *J Geophys Res Space Phys* 123(10):8749–8765. <https://doi.org/10.1029/2018JA025367>
- Kumar S (2020) Equatorial ionospheric TEC and scintillations under the space weather events of 4–9 September 2017: M-class solar flares and a G4 geomagnetic storm. *J Atmos Sol-Terr Phys* 209:105421. <https://doi.org/10.1016/j.jastp.2020.105421>
- Lei J, Huang F, Chen X, Zhong J, Ren D, Wang W, Xue X (2018) Was magnetic storm the only driver of the long-duration enhancements of daytime total electron content in the Asian-Australian sector between 7 and 12 September 2017? *J Geophys Res Space Phys* 123(4):3217–3232. <https://doi.org/10.1029/2017JA025166>
- Li G, Ning B, Wang C, Abdu MA, Otsuka Y, Yamamoto M, Chen J (2018) Storm-enhanced development of postsunset equatorial plasma bubbles around the meridian 120°E/60°W on 7–8 September 2017. *J Geophys Res Space Phys* 123(9):7985–7998. <https://doi.org/10.1029/2018JA025871>
- Liu J, Zhang D, Coster AJ, Zhang S, Ma G, Hao Y, Xiao Z (2019) A case study of the large-scale traveling ionospheric disturbances in the eastern Asian sector during the 2015 St. Patrick's day geomagnetic storm. *Ann Geophys* 37(4):673–687. <https://doi.org/10.5194/angeo-37-673-2019>
- Liu L, Zou S, Yao Y, Aa E (2020a) Multi-scale ionosphere responses to the May 2017 magnetic storm over the Asian sector. *GPS Solut* 24(26):1–15. <https://doi.org/10.1007/s10291-019-0940-1>
- Liu Y, Li Z, Fu L, Wang J, Zhang C (2020b) Studying the ionospheric responses induced by a geomagnetic storm in September 2017 with multiple observations in America. *GPS Solut* 24(1):1–13. <https://doi.org/10.1007/s10291-019-0916-1>
- Lyons LR, Nishimura Y, Zhang S, Coster AJ, Bhatt A, Kendall E, Deng Y (2019) Identification of auroral zone activity driving large-scale traveling ionospheric disturbances. *J Geophys Res Space Phys* 124(1):700–714. <https://doi.org/10.1029/2018JA025980>
- Matamba TM, Habarulema JB, McKinnell LA (2015) Statistical analysis of the ionospheric response during geomagnetic storm conditions over South Africa using ionosonde and GPS data. *Space Weather* 13(9):536–547. <https://doi.org/10.1002/2015SW001218>
- Tang J, Yao Y, Zhang L (2015) Temporal and spatial ionospheric variations of April 20 2013 Earthquake in Yaan. *China IEEE Geosci Remote S* 12(11):2242–2246. <https://doi.org/10.1109/lgrs.2015.2463081>
- Tang J, Yao Y, Kong J, Zhang L (2016) Large-scale traveling ionospheric disturbances using ionospheric imaging at storm time: a case study on March 17 2013. *J Atmos Sol-Terr Phys* 145:12–20. <https://doi.org/10.1016/j.jastp.2016.04.006>
- Wen D, Mei D (2020) Ionospheric TEC disturbances over China during the strong geomagnetic storm in September 2017. *Adv Space Res* 65(11):2529–2539. <https://doi.org/10.1016/j.asr.2020.03.002>
- Yao Y, Liu L, Kong J, Zhai C (2016) Analysis of the global ionospheric disturbances of the March 2015 great storm. *J Geophys Res Space Phys* 121(12):12157–12170. <https://doi.org/10.1002/2016JA023352>
- Yasyukevich Y, Astafyeva E, Padokhin A, Ivanova V, Syrovatskii S, Podlesnyi A (2018) The September 6 2017 X-class solar flares and their impacts on the ionosphere, GNSS, and HF radio wave propagation. *Space Weather* 16(8):1013–1027. <https://doi.org/10.1029/2018SW001932>
- Zakharenkova I, Astafyeva E, Cherniak I (2016) GPS and GLONASS observations of large-scale traveling ionospheric disturbances during the 2015 St. Patrick's day storm. *J Geophys Res Space Phys* 121(12):12–138. <https://doi.org/10.1002/2016JA023332>
- Zhang K, Li X, Xiong C, Meng X, Li X, Yuan Y, Zhang X (2019a) The influence of geomagnetic storm of 7–8 September 2017 on the Swarm precise orbit determination. *J Geophys Res Space Phys* 124(8):6971–6984. <https://doi.org/10.1029/2018JA026316>
- Zhang S, Coster AJ, Erickson PJ, Goncharenko LP, Rideout W, Vierinen J (2019b) Traveling ionospheric disturbances and ionospheric perturbations associated with solar flares in September 2017. *J Geophys Res Space Phys* 124(7):5894–5917. <https://doi.org/10.1029/2019JA026585>

Publisher's Note Springer Nature remains neutral with regard to jurisdictional claims in published maps and institutional affiliations.



Jun Tang received a B.S. and M.S. degree in geodesy and surveying engineering from the East China University of Technology, Fuzhou, China, in 2006 and 2009, respectively, and the Ph.D. degree in geodesy and surveying engineering from Wuhan University, Wuhan, China, in 2014. He is an Associate Professor with the School of Civil Engineering and Architecture, East China Jiaotong University, Nanchang, China. His research interests include Global Navigation Satellite Systems (GNSS) data

processing, ionospheric modeling using GNSS data, and multidimensional ionospheric tomography based on GNSS observations and GNSS applications.



Xin Gao received a B.S. degree in traffic engineering from the School of Highway, Chang'an University, Xi'an, China, in 2018. He is pursuing a M.S. degree from the School of Civil Engineering and Architecture, East China Jiaotong University, Nanchang, China. His main interests are Global Navigation Satellite Systems (GNSS) data processing and ionospheric modeling using GNSS data.



Yinjian Li received a B.S. degree in surveying and mapping engineering from the Shijiazhuang Tiedao University, Shijiazhuang, China, in 2017. He is currently a master's student in the School of Civil Engineering and Architecture, East China Jiaotong University, Nanchang, China. His research interests mainly include high-precision GNSS data processing and ionospheric data assimilation.



Zhengyu Zhong received a B.S. degree in traffic engineering from Shenzhen University, Shenzhen, China, in 2020. He is pursuing an M.S. degree in the School of Civil Engineering and Architecture, East China Jiaotong University, Nanchang, China. His research interests mainly include ionospheric modeling.